Water Science & Technology

IWA PUBLISHING

Water Science & Technology Vol 85 No 9, 2463 doi: 10.2166/wst.2022.128

Effective adsorption of antimony (V) from contaminated water by a novel composite manganese oxide/oxyhydroxide as an adsorbent

L. X. Xie[a], Y. Zhong[b,*], Y. Y. Chen[b], G. Y. Zhou[a] and C. Yang[a]

[a] Hunan Key Laboratory of Biomedical Nanomaterials and Devices, College of Life Sciences and Chemistry, Hunan University of Technology, Zhuzhou 412007, China
[b] Key Laboratory of Water Pollution Control Technology, Hunan Research Academy of Environmental Sciences, Changsha 410004, China
*Corresponding author. E-mail: zhongyu@hnu.edu.cn

ABSTRACT

To obtain an efficient and low-cost adsorbent for the Sb(V) removal in Sb(V)-contaminated water, a novel composite manganese oxide/oxyhydroxide (CMO) was synthesized by a simple hydrothermal synthesis method. The synthesized adsorbent was characterized via scanning electron microscopy, X-ray diffraction, transmission electron microscopy, Brunauer–Emmett–Teller surface area, Fourier transform infrared, and X-ray photoelectron spectroscopy analyses. The results revealed that the as-prepared CMO adsorbent possessed a porous structure consisting of Mn_3O_4 nanoparticles and MnOOH nanorods. Batch experiments showed that the adsorption behaviours were well fitted by the Langmuir isotherm and the pseudo-second-order kinetic model, reaching the maximum adsorption capacity of 119.63 mg/g at 25 °C. The application of CMO adsorbent showed that the Sb(V) removal efficiency in 6.24 L Sb(V)-containing water with a concentration of 3.6 mg/L was more than 90%. The reusability of CMO adsorbent demonstrated that the Sb(V) removal efficiency was still more than 80% even after five times of regeneration. The adsorption mechanism for Sb(V) can be described as ligand exchange between hydroxyl groups on the adsorbent surface and hydroxyl groups in $Sb(OH)_6^-$ molecules by forming inner-sphere complexes. Those results suggested that the CMO adsorbent can be considered as a potential adsorbent to remove Sb(V) from contaminated water.

Key words: adsorption behaviour, adsorption mechanism, composite manganese oxide/oxyhydroxide, Mn_3O_4 nanoparticles, MnOOH nanorods, Sb(V)

HIGHLIGHTS

- A novel composite manganese oxide/oxyhydroxide (CMO) adsorbent was synthesized.
- The CMO adsorbent was composed of Mn_3O_4 nanoparticles and MnOOH nanorods.
- It can be a potentially promising adsorbent to removal Sb(V).

INTRODUCTION

Antimony (Sb) is a metalloid that has both metallic and nonmetallic properties. Release of Sb into the environment is related to both natural processes (rock weathering, sedimentation, etc.) (Wedepohl 1995) and human activities (mining, smelting, combustion, etc.) (Filella *et al.* 2002). It is reported that dissolved Sb concentrations in pollution-free systems are usually less than 1 μg/L (Filella *et al.* 2002). High concentrations of Sb in air, soil and water bodies have been reported near mining areas, smelter plants and other Sb-containing product sites (Scheinost *et al.* 2006; Foster *et al.* 2019). For instance, water samples from a mine area (Xikuangshan antimony mine of Hunan Province, China) were found to be contaminated with Sb concentration of up to 6,384 μg/L, which is three orders of magnitude above the natural background (Wang *et al.* 2011). More attention has been focused on antimony pollution because of the growing awareness of its risk to human health, such as respiratory irritation, pneumoconiosis, antimony spots on the skin and gastrointestinal symptoms (Sundar & Chakravarty 2010). Both the Environmental Protection Agency of the United States (USEPA) (Callahan *et al.* 1979) and the European Union (Council of the European Communities) (EEC 1976) have included Sb as a priority contaminant. The former even recommended a level of 6 μg/L as the maximum contamination concentration of Sb in drinking water (USEPA 2009).

In natural environments (waters, soil and sediments), the inorganic Sb usually exists in two oxidation states, namely trivalent antimony (Sb(III)) and pentavalent antimony (Sb(V)). It heavily depends on the ambient environmental conditions (Filella & May 2003). Sb(III) is generally present under reducing conditions, where it abundantly exists in the form of the antimonous acid $Sb(OH)_3$ with pKa = 11.9 (Mitsunobu *et al.* 2010). Sb(V) exists under oxic environments, where it predominates as the deprotonated form of $Sb(OH)_6^-$ (the pH value ranges from 2 to 11) (Filella *et al.* 2002). The toxicity of Sb can effectively be reduced by the oxidation of Sb(III) to Sb(V) through biogeochemical or chemical oxidation (Chen *et al.* 2003). However, the oxidation of Sb(III) leads to the release of Sb(V) as the dominant sorbed species in sediment. It proved to be more difficult to remove Sb(V) than Sb(III) by either adsorption or coagulation (Guo *et al.* 2009). Thus, it becomes an urgent requirement to develop feasible adsorbents with high adsorption capacity, chemical stability and low cost for Sb(V) removal from water.

There have been many studies devoted to the development of effective methods for removing heavy metal or toxic substances from contaminated water, including electrodeposition (Mosivand *et al.* 2018; Nepel *et al.* 2019), reverse osmosis (Yang *et al.* 2017), precipitation/coagulation (Park *et al.* 2017; Liu *et al.* 2019), adsorption (Elgarahy *et al.* 2020; Elwakeel *et al.* 2021; Shalaby *et al.* 2021) and membrane filtration (Garba *et al.* 2019). Among those methods, adsorption is hailed as one of the most potential treatment methods due to its advantageous properties in terms of flexibility, ease of operation, cost-effectiveness and eco-friendliness (Long *et al.* 2020). The adsorption behaviour of Sb on various adsorbents, such as metal oxides (Thanabalasingam & Pickering 1990; Wang *et al.* 2019a), inorganic minerals (Qiu *et al.* 2018), carbon-based materials (Luo *et al.* 2015a; Jiang *et al.* 2020) etc., has been elaborated. Manganese (Mn) oxides (or oxyhydroxides), such as manganese dioxide (MnO_2) and manganese oxyhydroxide (MnOOH), can provide a large accessible surface area and potentially serve as an important adsorbent for environmental pollutants. Batch equilibrium experiments combined with various spectroscopic techniques have suggested specific Sb(V) adsorption at the edge sites of δ-MnO_2 by forming a monodentate mononuclear complex (Sun *et al.* 2018). However, MnO_2 suffers from an inherent limitation of the low removal efficiency due to the low affinity of MnO_2 to Sb. Although Mn-related binary oxides were proved to have high adsorption capacity for the Sb removal in wastewater treatment, Mn oxides mainly accounted for the Sb(III) oxidation rather than the Sb(V) removal (Xu *et al.* 2011). Therefore, there are still some challenges in improving the adsorption capacity and accelerating the adsorption process of Mn oxides during the Sb(V) removal.

Thus in this paper, a new composite manganese oxide (CMO) was synthesized by a simple hydrothermal synthesis method in our laboratory. It can be expected as a potentially promising adsorbent to remove Sb(V) from contaminated water. The objectives of the study are: (I) to identify the construction of the CMO adsorbent; (II) to determine the adsorption characteristics of the CMO adsorbent by the adsorption isotherms and thermodynamics; (III) to study the influence of different conditions on the Sb(V) adsorption, including pH, coexisting anions, etc.; and (IV) to investigate the Sb(V) adsorption mechanism by the CMO adsorbent.

MATERIALS AND METHODS

Materials and chemicals

Manganese powder (Mn, 2N grade), potassium antimonite [$KSb(OH)_6$], potassium permanganate, manganese sulfate monohydrate, sodium carbonate, sodium bicarbonate, sodium sulfate, sodium nitrate, sodium hydroxide, and ethanol were brought from Sinopharm Chemical Reagent Co., Ltd (Shanghai, China) and all chemical reagents were of analytical grade. All solutions were prepared using deionized water with a resistivity of 18 MΩ cm (Millipore Corp., Billerica, USA). Sb(V) stock solution was obtained by dissolving $KSb(OH)_6$ and 2 M HCl in an appropriate amount of deionized water.

Synthesis and characterization

Potassium permanganate ($KMnO_4$) and hydrate manganese sulfate ($MnSO_4{\cdot}H_2O$) were separately dissolved into deionized water at room temperature in a ratio of 2:3 (substance amount). The potassium permanganate solution was dropwise added to the hydrate manganese sulfate under magnetic stirring. After stirring for 3 h, the resulting homogeneous solution was transferred into an autoclave and subjected to hydrothermal treatment at a constant temperature of 160 °C for 6 h. After the reaction was completed, the suspension was taken out and cooled down to room temperature naturally. The product was centrifuged and repeatedly washed with deionized water to get rid of the remaining ions, and finally dried at 110 °C to obtain nano-manganese dioxide.

The CMO adsorbent was prepared using the following hydrothermal synthesis procedures. The manganese powder was prepared by finely grinding and sieving in advance and then mixed with the synthesized nano-MnO_2 in deionized water. After stirring at room temperature for 1 h, the solution was heated to 65 °C and kept for another 6 h. Subsequently, the resulting mixed precipitate was ultrasonically dispersed for 30 minutes and further filtered, followed by repeatedly washing with deionized water. After drying treatment at 60 °C, the resulting powder was stored under nitrogen protection for further experiments.

Morphologies of the CMO adsorbent were collected by scanning electron microscopy (SEM, Nano SEM-4800, HITACHI, Japan). The elemental analyses were performed using an Energy-dispersive System (EDS). The phase composition in the CMO adsorbent was analysed using an x-ray diffractometer (XRD, Smart Lab 3KW, Japan). The specific surface area and the pore size distribution were determined by the Brunauer–Emmett–Teller (BET, Quadrasorb EVO, USA) N_2 adsorption/desorption method and the Brunauer–Joyner–Hallenda (BJH) method. Both the Fourier transform infrared spectrometer (FTIR, Nicolet iS50, USA) and the X-ray photoelectron spectroscope (XPS, Thermo Escalab 250Xi, USA) were applied to analyse the structures of the samples before and after Sb(V) adsorption.

Batch adsorption experiments

The adsorption isotherms of Sb(V) were carried out at varying temperatures (i.e., 25, 35 and 45 °C). 0.05 g of CMO adsorbent was added into a conical flask containing 100 mL of Sb(V) solutions with different initial concentrations (ranging from 2 to 100 mg/L). In each test, the solution pH was controlled to 7.0 $\pm$ 0.1 by acid-base buffer solution, and the ionic strength was maintained with 100 mg/L Na_2CO_3. The flasks were shaken on a shaker (BS-2E, Changzhou, China) at a certain temperature for 12 h. Then, all the samples were filtered by 0.45 μm membrane and analysed for residual antimony by the AFS-8230 atomic fluorescence spectrophotometer (Beijing Yoshida, China).

In adsorption kinetics experiments, 0.5 g of CMO adsorbent was added into a 1,000 mL solution with an initial Sb(V) concentration of 10 mg/L. 100 mg/L Na_2CO_3 was used to control background ionic strength at a constant level, and the solution pH was controlled to 7.0 $\pm$ 0.1 by acid-base buffer solution. The kinetics experiments were conducted at 25 °C with shaking at 160 rpm in a shaker. To determine the remaining antimony, a small aliquot of aqueous samples was taken and filtered through a 0.45 μm membrane at a specific time interval from 5 min to 10 h.

In order to explore the effect of solution pH on Sb adsorption, adsorption experiments were performed at various pH values. 0.05 g of CMO adsorbent was added into 100 mL solution with an initial Sb(V) concentration of 10 mg/L and a constant level of ionic strength. Because the dominant Sb(V) species is $Sb(OH)_6^-$ as the pH value ranges from 2.7 to 10.4, the pH in those adsorption experiments was manually controlled in the range of 3.0–10.0 using 0.1 M acid-base buffer solution. The solutions were shaken at 160 rpm for 6 h when the temperature was set at 25 °C.

To investigate the influence of commonly co-existing anions (SO_4^{2-}, NO_3^-, PO_4^{3-} and HCO_3^-) and humic acid on the adsorption process, 0.05 g of CMO adsorbent was added into 100 mL Sb(V)-containing solution with relevant anion concentrations (ranging from 0 to 500 mg/L). The initial Sb(V) concentration was 10 mg/L, and the pH was controlled to 7.0 $\pm$ 0.1 by 0.1 M acid-base buffer solution. The experiments were performed with constantly shaking at 160 rpm for 6 h at a constant temperature (25 °C). Moreover, the blank sample was prepared in a similar way without adding coexisting anion.

The regeneration of adsorbents is an important aspect since it determines whether an adsorbent can be brought into practical application. A total of four consecutive adsorption/desorption of the Sb(V) processes were performed in triplicate to evaluate the reusability of the CMO adsorbent. The saturated adsorbent was respectively soaked in different solutions, including deionized water, 0.1 mol/L HNO_3, 0.1 mol/L citric acid, 0.1 mol/L NaCl and 0.019 g/L EDTA, and then shaken at 160 rpm for 6 h at a specific temperature (three levels, i.e., 25, 35 and 45 °C). After high-speed centrifugation for 10 minutes, the supernatant was taken to determine the content of Sb in solution for calculating the desorption rate. The resulting adsorbents, after being washed with deionized water at least three times, were dried in an oven at 60 °C for use in the next cycle.

RESULTS AND DISCUSSION

Characterization of CMO adsorbent

As displayed by the XRD in Figure 1(a), there are two dominant manganese oxide(s)/oxyhydroxide(s), i.e., Mn_3O_4 and MnOOH, existing in the as-prepared CMO adsorbent. The strong peaks at 18.01°, 28.89°, 31.01°, 32.31°, 36.08°, 44.45°,

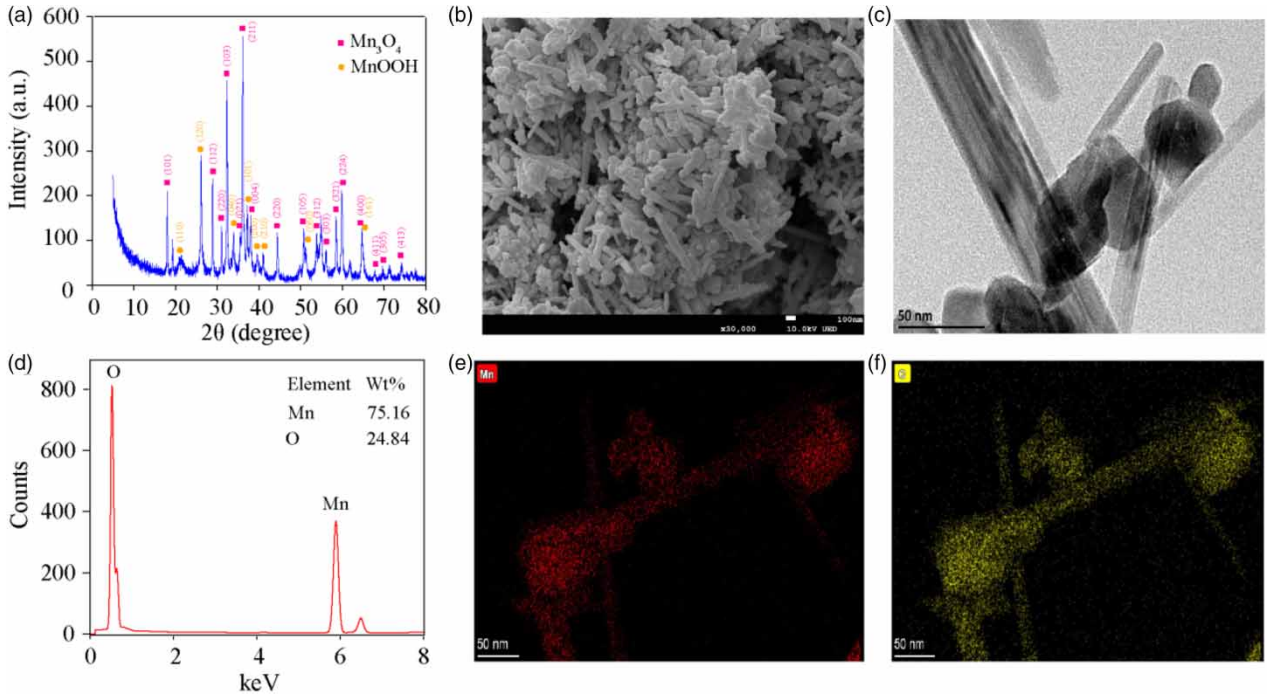

Figure 1 | Characterization of CMO adsorbent: (a) X-ray diffraction patterns, (b) SEM, (c) TEM and (d) EDS spectra of CMO; (e) and (f) Elemental mapping images of CMO.

50.71°, 58.51° and 59.84 are attributed to (101), (112), (200), (103), (211), (220), (105), (321) and (224) planes of the structure of Mn_3O_4 (PDF#24-07343), respectively. Other observed peaks at 25.66°, 33.54°, 37.11°, and 64.72° are indicative of MnOOH (PDF#12-0733). The EDS spectrum for determining the specific elemental contents is depicted in Figure 1(d), which indicates the presence of the expected elements in the prepared CMO adsorbent, i.e., manganese and oxygen (hydrogen is not included in EDS). The elemental analysis of the CMO adsorbent identified the weight percentage of manganese and oxygen as 75.16% and 24.84%, respectively. Further structural characterization of the CMO adsorbent was analysed by the SEM-mapping as shown in Figure 1(e) and 1(f). The mapping shapes of the CMO adsorbent regarding Mn and O elements show that the prepared adsorbent possesses a characteristic of uniform element composition and dispersion.

The SEM and transmission electron microscopy (TEM) images were collected to confirm the morphology of the prepared CMO adsorbent, as displayed in Figure 1(b) and 1(c). It reveals that the CMO adsorbent is aggregated, consisting of nanoparticles and nanorods. According to the hydrothermal synthesis results reported by Hu (Hu *et al.* 2008), the nanoparticles and nanorods can be identified as Mn_3O_4 and MnOOH, respectively. The TEM image shows that Mn_3O_4 nanoparticles have an average size of 30 nm, most of which are nanocubes. Nanorods of MnOOH are formed with diameters of 10–50 nm and lengths of hundreds of nanometres. The large quantity of Mn_3O_4 nanoparticles and MnOOH nanorods in Figure 1(b) further demonstrates success in synthesizing composite oxide via a simple hydrothermal method. The aggregation of numerous Mn_3O_4 nanoparticles on MnOOH nanorods results in the presence of a porous structure, which is advantageous for the target species to adsorb on its surface. The specific surface area (BET) by nitrogen adsorption-desorption measurements was then used to determine the surface properties of CMO adsorbent, and the results are shown in Figure 2. According to the IUPAC classification, the CMO adsorbent exhibits the type-IV isotherm with a type-H3 hysteresis loop when the relative pressure (P/P0) ranges from 0.4 to 1.0. It implies a typical mesoporous structure in the CMO adsorbent. The surface area and pore size of the CMO adsorbent are 30.860 m^2/g and 8.7 nm, respectively. It means that the high specific surface areas could provide considerable surface active sites for diffusion and adsorption of adsorbent.

Adsorption isotherms

When the pH value is 7.0 $\pm$ 0.1, the adsorption isotherms of Sb(V) on CMO adsorbent at 298, 308 and 318 K are depicted in Figure 3. With the increase of initial concentration, there has been a rapid increase in the adsorption amounts of Sb(V) on the

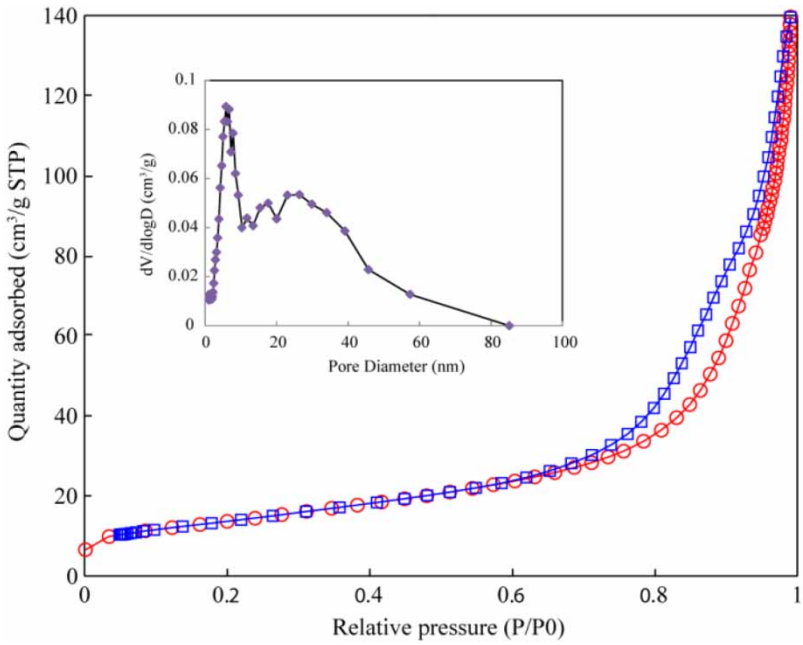

Figure 2 | N_2 adsorption-desorption isotherms of CMO adsorbent.

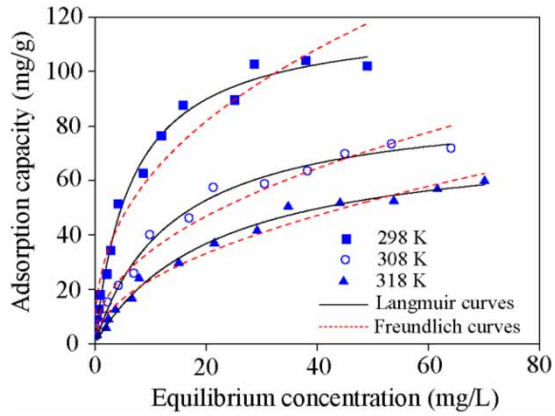

Figure 3 | Adsorption isotherm of Sb(V) on the CMO adsorbent at different temperatures. The initial Sb(V) concentration was 2–100 mg/L; the adsorbent dose was 0.5 g/L; the solution volume was 100 mL.

CMO adsorbent and then a slow rise tendency. Besides, the adsorption capacity of Sb(V) on the CMO adsorbent exhibits a downward trend as the temperature increases, indicating that the adsorption process is exothermic.

The equilibrium adsorption isotherm data were subjected to model analysis by both Langmuir and Freundlich isotherms:

$$\frac{C_e}{q_e} = \frac{1}{k_l q_m} + \frac{C_e}{q_m} \tag{1}$$

$$q_e = k_F C_e^{1/n} \tag{2}$$

where q_e (mg/g) and C_e (mg/L) are the amount of Sb(V) adsorbed on the CMO adsorbent and the Sb(V) concentration in the water samples at equilibrium, respectively. In Equation (1), q_m (mg/g) refers to the maximum adsorption capacity of adsorbents; k_l (L/mg) is the Langmuir isotherm constant, which reflects the power of adsorption experiments. Meanwhile, in Equation (2), k_F [(mg/g) (L/mg)$^{1/n}$] and n is the Freundlich isotherm constant.

Table 1 | Langmuir and Freundlich parameters for Sb(V) adsorption on the CMO adsorbent

	Langmuir model			Freundlich model		
Temperature (K)	q_m (mg/g)	k_l (L/mg)	R^2	n	k_F ($mg^{1-(1/n)}L^{1/n}g^{-1}$)	R^2
298	119.63	0.1503	0.9914	2.46	24.2412	0.9441
308	89.29	0.0722	0.9906	2.17	11.8601	0.9623
318	76.43	0.0464	0.9901	1.98	7.3746	0.9755

The relevant parameters regarding the Sb(V) isotherms at different temperatures are presented in Table 1. According to the correlation coefficient (R^2) values, the Langmuir model should be superior to the Freundlich model. For the Langmuir model, the adsorption site energy is generally considered to be a constant, and the adsorption can reach a maximum when all sorption sites are occupied as a single layer. The theoretical adsorption capacity of CMO obtained by the Langmuir model is 119.63 mg/g at 25 °C.

A comparison of adsorption capacities of other adsorbents for Sb(V) is listed in Table 2. Notably, it is not easy to compare the prepared adsorbents with other adsorbents due to different experimental conditions. The average concentration in actual Sb(V)-contaminated water is usually not too high, and hence, the adsorption capacity of the adsorbent is required to be better at low concentration. The prepared CMO adsorbent exhibits relatively high sorption capacity compared with other adsorbents for Sb(V) at the low concentration. The adsorption of Sb(V) on the CMO adsorbent gradually reached equilibrium in about 200 min. The equilibrium time is considerably faster than other new nanocomposites, such as Mn-coated biochar, which reach equilibrium in about 1,200 min. Compared to adsorbents consisting of expensive ingredients like Co_3O_4@rGO, the CMO adsorbent can be synthesized by cheap and readily available materials, which is very critical for technology popularization. Therefore, the comprehensive features and properties make CMO a promising adsorbent for removing Sb(V) in practical application.

In order to determine the nature of the adsorption process (physical or chemical), the adsorption data were further fitted by the Dubinin–Radushkevich (D-R) isotherm model (Luo *et al.* 2015b), which is expressed as below:

$$\ln q'_e = \ln q'_m - \beta\varepsilon^2 \tag{3}$$

where q'_e (mol/g) refers to the amount of Sb(V) sorbed per unit weight of adsorbent; q'_m (mol/g) represents the maximum adsorption capacity; β (mol^2/J^2) corresponds to the activity coefficient associated with the mean free energy of adsorption; ε represents the Polanyi potential, which can be calculated by the equation of $\varepsilon = RT\ln(1 + 1/C_e)$.

Table 2 | Comparison of adsorption capacities of various adsorbents for Sb(V)

Adsorbent	q_e (mg/g)	Concentration (mg/L)	Equilibrium time (min)	Dose (g/L)	Reusability performances	Ref.
BM-ZVI/FeS_2	248.1	20–600	180	0.5	–	He *et al.* (2020)
Ce/Fe_{CP}-BC	25.0	10–100	560	1.0	–	Wang *et al.* (2019b)
Co_3O_4@rGO	152.6	10–300	240	1.0	–	Jiang *et al.* (2020)
CNT-Fe(0)	250.0	10–300	200	0.5	80% [5 cycles]	Mishra *et al.* (2016)
MB80	0.73	50	1,200	50.0	–	Jia *et al.* (2020)
Ce-doped Fe_3O_4	188.1	10–100	360	0.2	100% [3 cycles]	Qi *et al.* (2017)
ZCN	57.17	10–500	50	1.0	–	Luo *et al.* (2015a)
RGO/Mn_3O_4	105.50	10–1000	125	1.0	–	Zou *et al.* (2016)
TiO_2 NTs	65.3	0.01–10	360	0.1	85% [4 cycles]	Zhao *et al.* (2019)
CMO	119.63	2–100	200	0.5	80% [5 cycles]	In this work

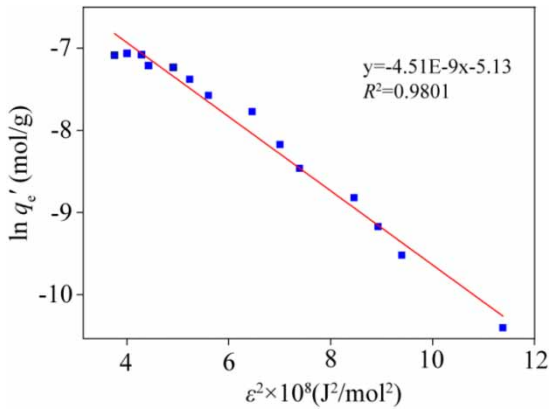

Figure 4 | Plot of ln*K* versus 1/*T* for the adsorption of Sb(V) on the CMO adsorbent.

The linear regression of $\ln q_e'$ vs ε^2 is shown in Figure 4. The R^2 value of 0.9931 implies that the D-R isotherm model describes the equilibrium data well. The q_m' value derived from the intercept of the plot is 5.9×10^{-3} mol/g. The mean free energy adsorption E (kJ/mol) (Luo *et al.* 2015a) can be obtained by the following equation:

$$E = \frac{1}{\sqrt{2\beta}} \tag{4}$$

The information regarding the type of adsorption process, whether chemical or physical, can be judged from the E value. The mean energy of the physical adsorption is recognized to be less than 8 kJ mol^{-1}, whereas it is higher than 8 kJ mol^{-1} for the chemical adsorption (Helfferich 1962). With respect to the Sb(V) adsorption on the CMO adsorbent, the E value is calculated as 10.53 kJ mol^{-1}, meaning that the adsorption of Sb(V) on the CMO adsorbent is a chemical process.

To further understand the thermodynamic property of the Sb(V) adsorption process, three fundamental thermodynamic parameters, i.e., standard Gibbs free energy ΔG (kJ mol^{-1}), standard enthalpy change ΔH (kJ mol^{-1}) and standard entropy change ΔS (J mol^{-1} K^{-1}), were calculated from the isotherm data by the following equations (Luo *et al.* 2015a):

$$\Delta G = -RT\ln K \tag{5}$$

$$\ln K = \frac{\Delta S^0}{R} - \frac{\Delta H^0}{RT} \tag{6}$$

where K refers to a dimensionless constant related to the thermodynamic equilibrium. In the case of diluted solution, it can be obtained by converting the Langmuir equilibrium constant k (L mg^{-1}) into L g^{-1}, subsequently making the multiplication by both the molecular weight of the adsorbate M (g mol^{-1}) and the unitary standard concentration of the adsorbate (1 mol L^{-1}) (Lima *et al.* 2018).

Based on the above equations, the ΔG parameters are determined as −24.33 kJ mol^{-1}, −22.51 kJ mol^{-1} and −21.42 kJ mol^{-1} for 298, 308 and 318 K, respectively. The decreasing trend in negative ΔG values with the increase of temperature implies that the degree of spontaneity declines as temperature increases. In the equation, the ΔH^0 and ΔS^0 parameters can be derived from the slope and intercept of the ln K versus $1/T$ plot. The results are listed in Table 3. The negative ΔH value

Table 3 | Thermodynamic parameters calculated for Sb(V) adsorption on the CMO adsorbent at different temperatures

T (K)	ln*K*	Δ*G* (kJ mol^{-1})	Δ*H*⁰ (kJ mol^{-1})	Δ*S*⁰ (J mol^{-1} K^{-1})
298	9.81	−24.33	−32.21	−27.83
308	9.08	−22.51		
318	8.64	−21.42		

(-32.21 kJ mol^{-1}) further demonstrates that the adsorption process is exothermic, which is in accordance with a decrease in the adsorption capacity with the increasing temperature. The negative ΔS value (-27.83 J mol^{-1} K^{-1}) implies decreased degrees of freedom of the adsorbed species.

Adsorption kinetics

Adsorption kinetics is critical when evaluating the adsorption process. The kinetics of Sb(V) adsorbed on the CMO adsorbent was studied. The result is displayed in Figure 5. It is obvious that the adsorption kinetics is rapid initially within 50 min and then slows down until the adsorption equilibrium. There are considerable adsorption sites available for Sb(V) adsorption at the beginning of the adsorption process. When the adsorption reaches a certain level, it is difficult for the remaining adsorption sites to be occupied due to the repulsive forces between the surface molecules on the CMO adsorbent and adsorbate solution. The adsorption equilibrium is reached after 200 min with the adsorption capacity of nearly 19.80 mg/g.

To further understand the adsorption behaviour, the adsorption kinetic data of Sb(V) on the CMO adsorbent was subjected to kinetic fitting, including the pseudo-first-order and pseudo-second-order models:

$$q_t = q_e(1 - e^{-K_1 t}) \tag{7}$$

$$q_t = \frac{q_e^2 K_2 t}{1 + q_e K_2 t} \tag{8}$$

where q_e and q_t correspond to the amount of adsorbate at equilibrium (mg/g) and at time t (min), respectively; and K_1 (min^{-1}) and K_2 (g mg^{-1} min^{-1}) refer to the rate constants for the pseudo-first- and pseudo-second-order model, respectively.

All the kinetics parameters were determined and listed in Table 4. The correlation coefficient ($R^2 = 0.9960$) of the pseudo-second-order model is superior to that ($R^2 = 0.9820$) of the pseudo-first-order model. The result suggests that the pseudo-

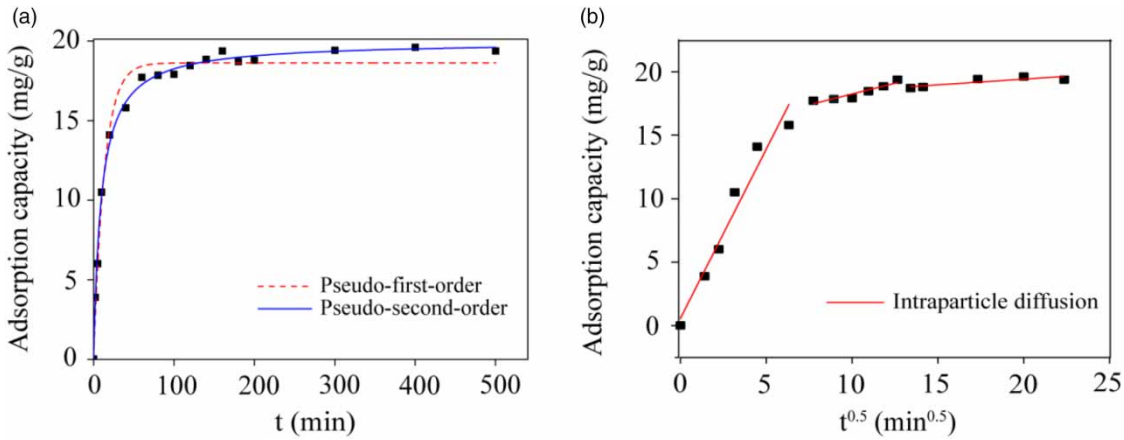

Figure 5 | Adsorption kinetics for Sb(V) adsorption on CMO adsorption fitted with (a) pseudo-first, pseudo-second-order models and (b) intraparticle diffusion model. The initial Sb(V) concentration was 10 mg/L; the adsorbent dose was 0.5 g/L; the solution volume was 1,000 mL; the temperature was 25 °C.

Table 4 | Kinetics parameters of the adsorption of Sb(V) on the CMO adsorbent

Model	K (min^{-1})	q_e (mg/g)	R^2
Pseudo-first-order	0.0751	18.62	0.9820
Pseudo-second-order	0.0053	19.97	0.9960
Intraparticle diffusion	K_{id} (mg/(g·min$^{0.5}$))	C (mg/g)	R^2
First phase	2.6630	0.5745	0.9561
Second phase	0.3378	14.8625	0.8908
Third phase	0.0905	17.6035	0.7223

second-order model can fit the equilibrium data more perfectly. Because chemisorption associated with sharing or exchange of electrons between sorbent and sorbate is recognized as the rate-limiting step in the pseudo-second-order kinetic model (Ye *et al.* 2011), the chemical adsorption, therefore, was the rate-controlling step in the Sb(V) sorption by the CMO adsorbent.

To further elucidate the diffusion mechanism of Sb(V) adsorbed on the CMO adsorbent, the intraparticle diffusion model (Weber & Morris 1963) was used to fit the experimental data. The intraparticle diffusion model can be written as:

$$q_t = K_{id} t^{1/2} \tag{9}$$

The curve-fitting plot is shown in Figure 5, and the fitting parameters are listed in Table 4. It can be seen that the plot can be separated into three phases, namely a sharp rise portion, a moderate increase and an equilibrium phase. Three different phases in the adsorption process indicate that the adsorption of Sb(V) on the CMO adsorbent is influenced by various independent steps, i.e., liquid film diffusion, intra-particle diffusion and adsorption reaction stage. During the liquid film diffusion, the Sb(V) is transferred to the external surface of the CMO adsorbent. Due to the high concentration of Sb(V) in the solution, there are abundant active sites on the surface of the adsorbent, and the adsorption rate is very high. Therefore, at this stage, Sb(V) diffusion is mainly limited by the pore structure of the CMO adsorbent. In the last equilibrium stage, the diffusion is primarily controlled by the Sb(V) already attached to the adsorbent, and the equilibrium adsorption of the CMO adsorbent is almost achieved.

Effect of pH on adsorption

The effect of initial solution pH on the Sb(V) adsorption was specifically investigated by varying pH from 3 to 10, as displayed in Figure 6. It can be seen that the adsorption of Sb(V) on the CMO adsorbent is heavily dependent on pH values. The maximum adsorption is obtained when the pH is less than 7.0. When the pH is higher than 7.0, the adsorption capacity drops dramatically. It can be attributed to a change in the positive charge on the surface of the adsorbent. When $pH < pH_{pzc}$ (zero point charge), the protonation of the adsorbent surface increases, leading to the increase of positive charge. Thus, the electrostatic attraction between $Sb(OH)_6^-$ and the charged surfaces is enhanced. When $pH > pH_{pzc}$, a more negative charge on the adsorbent surface enhanced the electrostatic repulsion forces between $Sb(OH)_6^-$ anions and charged surface, resulting in a decrease in the adsorption capacity. The results indicate that Sb(V) adsorption on the CMO adsorption is relatively efficient over a wide range of pH values (from 3.0 to 7.0), suggesting that the prepared CMO adsorbent has a great potential of application in natural water systems.

Besides, the leaching of the Mn element from the CMO adsorbent at different pH values was studied and displayed in Figure 6. The concentrations of Mn released in solutions change from 0.06 to 1.6 mg/L. According to the limits of Mn at 2.0 mg/L in the Discharge Standard of Pollutants for Municipal Wastewater Treatment Plant, the release of Mn element is negligible over a wide range of pH (from 3 to 10). It suggests that the prepared adsorbent exhibits favourable physical and

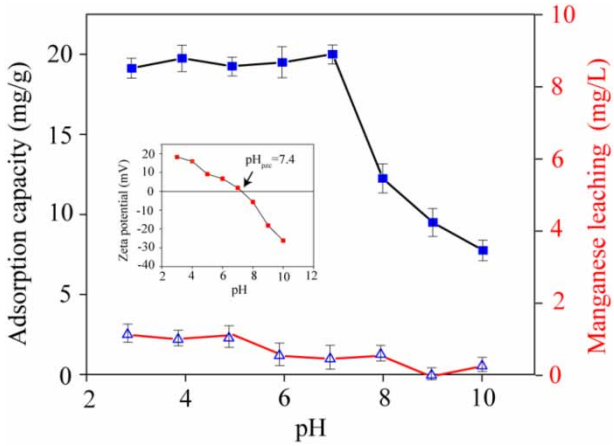

Figure 6 | Effect of pH (in the range of 3.0–10.0) on the adsorption capacity of Sb(V) on CMO adsorbent. The initial Sb(V) concentration was 10 mg/L; the adsorbent dose was 0.5 g/L; the solution volume was 100 mL; the temperature was 25 °C.

chemical stability. In this regard, the as-prepared CMO adsorbent has the potential for treating Sb(V)-containing water due to its stable structure and good security.

Effect of coexisting anions

The effects of commonly present anions (such as NO_3^-, HCO_3^-, SO_4^{2-} and PO_4^{3-}) and humic acid on the adsorption of Sb(V) by the CMO adsorbent were investigated at different concentrations (ranging from 0 to 500 mg/L). The results are described in Figure 7. The Sb(V) removal efficiency varies slightly with the anion concentration (NO_3^-, HCO_3^-, and SO_4^{2-}) and humic acid increasing from 0 to 500 mg/L. It indicates that these coexisting components do not greatly influence the Sb(V) adsorption. It has been reported that the adsorption involving the out-sphere surface complexes is highly sensitive to ion strength, since it was inhibited by weakly adsorbing anions through electrostatic competition (Mcbride 1997). On the contrary, the adsorption associated with inner-sphere surface complexes showed little sensitivity to ionic strength. In this respect, it suggests that the Sb(V) might be chemically adsorbed on the CMO adsorbent by forming inner-sphere surface complexes at the water/oxide interface. It is worth noting that the Sb(V) removal efficiency decreases sharply with the increasing concentration of PO_4^{3-}. As the concentration of PO_4^{3-} varies from 0 to 500 mg/L, the removal efficiency reduces to 30.8%. A similar interfering effect of phosphate on arsenic removal has been shown (Gupta *et al.* 2009). The significant decrease of Sb(V) removal efficiency in the presence of phosphate can be interpreted by the strong competition between phosphate and Sb(V) for adsorbent binding sites.

Reusability and application

The regeneration of the CMO adsorbent adsorbed with Sb(V) via various treatments (H_2O, HNO_3, citric acid, NaCl and EDTA) at different temperatures (25, 35 and 45 °C) has been evaluated, and the comparison results are displayed in Figure 8. It can be seen that the desorption capacity of EDTA is superior to others. The reason is that the amino and carboxyl groups in EDTA can form more stable complexes with Sb(V), and as a result, the adsorbed Sb(V) can be desorbed from the CMO adsorbent. In addition, it is worthwhile mentioning that the desorption capacities for all treatments gradually increase when the temperature varies from 25 °C to 45 °C, suggesting that the desorption process could be endothermic. Five adsorption-regeneration cycles for EDTA treatment were carried out, as depicted in the inset in Figure 8. Generally, the adsorption capacity of the adsorbent tends downwards with an increase in the regeneration cycle. However, it shows an unremarkable decrease for the CMO adsorbent, and the reduction in Sb(V) removal efficiency was only 7.0% even after the fifth regeneration. These results indicate that the prepared CMO adsorbent could be easily regenerated via EDTA treatment and used repeatedly. For comparison, reusability performances for several reported adsorbents are listed in Table 2. It can be seen that the prepared CMO adsorbent is comparable to other reported adsorbents.

For application, a self-made model device with a plexiglass column (350.0 mm × 50.0 mm) was built for Sb(V)-contaminated water treatment, as shown in Figure 9(a). The plexiglass column was filled with a small portion of gravel, a 100 mm

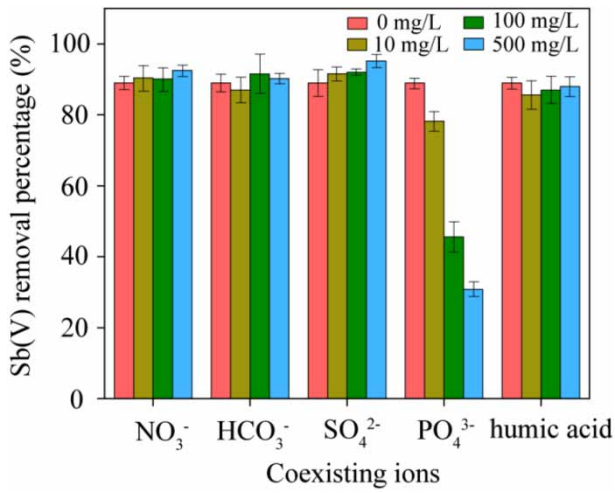

Figure 7 | Effects of the coexisting ions and humic acid on the removal of Sb(V) by CMO adsorbent. The initial Sb(V) concentration was 10 mg/L; the adsorbent dose was 0.5 g/L; the solution volume was 100 mL; the temperature was 25 °C.

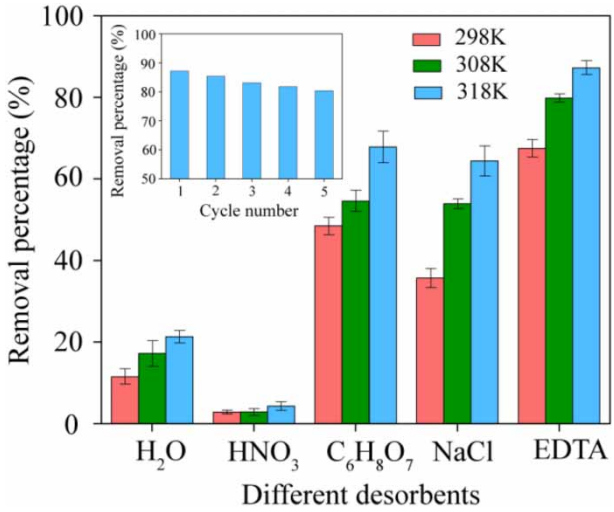

Figure 8 | Removal percentage of Sb(V) by CMO adsorbent after treatments of various desorbents at different temperatures (298 K, 308 K, 318 K) and specific EDTA-treating in five successive sorption-desorption cycles at 318 K (inset figure). The initial Sb(V) concentration was 10 mg/L; the adsorbent dose was 0.5 g/L; the solution volume was 100 mL.

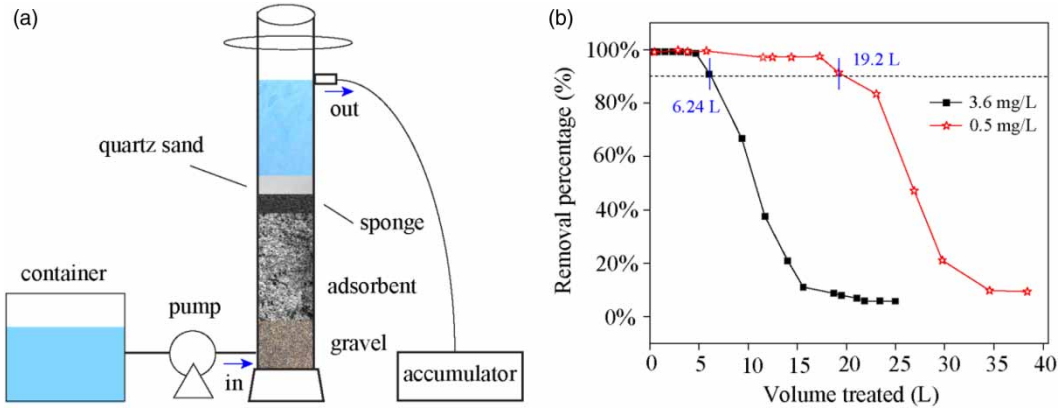

Figure 9 | Application in Sb(V)-pollutant water treatment: (a) self-made model device, (b) Sb(V) removal percentage after passing through the self-made model device.

column height of CMO adsorbent, and an appropriate amount of sponge as the bottom, middle, and upper layer, respectively. A certain amount of quartz sand was finally compacted at the top. When pumping Sb(V)-containing water into the column via a peristaltic pump, water will pass through the packing column from the bottom to the top. In the simulation experiment, Sb(V)-containing water with different concentration levels was continuously treated by this device with a flow rate of 6.5 mL/min. Figure 9(b) shows that 6.24 L of Sb(V)-containing water with a concentration of 3.6 mg/L can be treated with the Sb(V) removal efficiency of more than 90% via this device. As for the Sb(V) initial concentration of 0.5 mg/L, the removal volume of Sb(V)-containing water is up to 19.2 L. It indicates that the as-prepared CMO adsorbent has promising application potential in Sb(V)-pollutant water treatment.

Sorption mechanism

FTIR and XPS are generally recognized as powerful techniques in investigating surface interactions between adsorbates and adsorbents. The interactions between Sb(V) and the functional groups on the CMO adsorbent can be determined by the FTIR and XPS spectra, such as the characteristic peak shift and intensity change.

The FTIR spectra of the original CMO and after adsorbing Sb(V) were respectively collected and shown in Figure 10. The peaks at 3,435 cm^{-1} and 1,630 cm^{-1} in spectra correspond to the hydroxyl groups of physisorbed water molecules on the

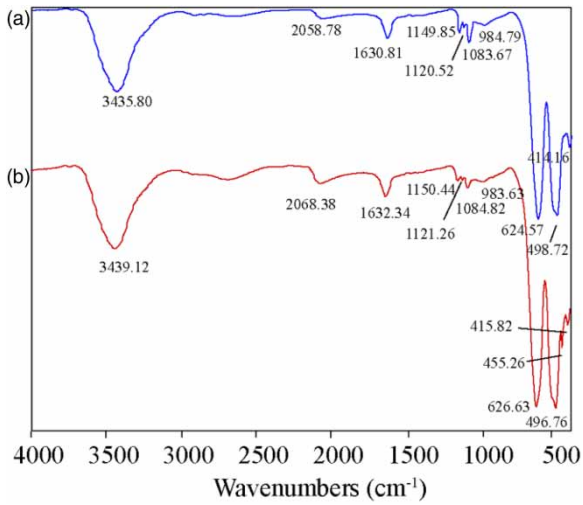

Figure 10 | FTIR spectra of the (a) original CMO adsorbent and (b) CMO adsorbent after adsorbing Sb(V).

adsorbents. Three peaks at 626, 496 and 415 cm^{-1} are associated with the vibration of Mn-O in Mn_3O_4, which is in agreement with previous FTIR studies of Mn_3O_4 (Ishii *et al.* 1972; Zhang *et al.* 2004). The peaks at 1,150, 1,120 and 1,084 cm^{-1} are attributed to the typical OH-bending modes of MnOOH: δ-1-OH, δ-2-OH and γ-OH, respectively (Zhang *et al.* 2004). The peaks related to bending vibration of hydroxyl groups on the adsorbent surface in wavenumber ranging from 900 to 1,200 cm^{-1} (Zhang *et al.* 2018) are not obvious because of the broad overlapping peaks in the region. But, the decreased intensity in the 900–1,200 cm^{-1} region of the spectrum after Sb(V) adsorption can be observed, indicating that the adsorption process involves cleavage of hydroxyl groups. It suggests that the hydroxyl groups on the adsorbent surface engage in Sb(V) sorption, and the hydroxyl groups in MnOOH molecules also possibly participate in the sorption process. Besides, a new peak appears at 455 cm^{-1} after adsorbing Sb(V), which can be attributed to the Sb(V)-O stretching vibration (Xu *et al.* 2011). Information regarding weakening and emerging peaks is indicative of the adsorption of Sb(V) on adsorbents by the formation of an inner sphere, as has been previously observed in studies of Sb(V) adsorption on MnO_2 (Liu *et al.* 2015).

To obtain further insight into the Sb(V) sorption on the CMO adsorbent, the chemical compositions of CMO before and after Sb(V) adsorption were measured by XPS. The O 1s, Sb 3d and Mn 2p spectra are illustrated in Figure 11. In the Mn 2p spectra, two peaks positioned at 530.6 eV and 539.9 eV are ascribed to Sb 3d5/2 and Sb 3d3/2, respectively (Luo *et al.* 2015a). The appearance of the Sb peak provides an indicator to determine that Sb(V) is adsorbed on the CMO adsorbent. The O 1 s spectrum of the CMO adsorbent in Figure 11(a) consists of three peaks positioned at the binding energy of 529.85 eV, 531.2 eV, and 531.9 eV, which can be assigned to metal oxide (M-O), hydroxyl bonded to metal (M-OH), and

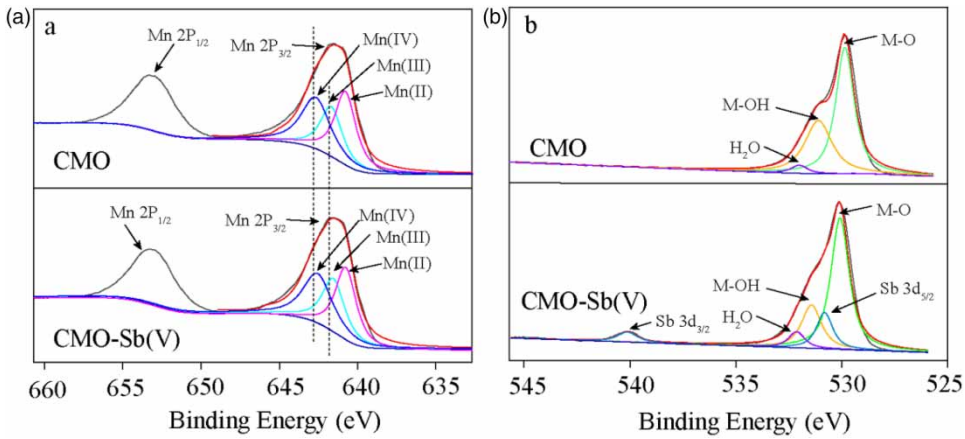

Figure 11 | XPS characterization of CMO adsorbent before and after Sb(V) adsorption. (a) Mn 2P, and (b) O 1s + Sb 3d.

adsorbed H_2O in the adsorbent (H_2O), respectively (Luo *et al.* 2015a). It shows that the area ratio for the peak at 531.1 eV (M-OH) decreases from 37.20% to 24.31% after Sb(V) adsorption. However, the area ratio of the peak at 529.85 eV (M-O) increases from 59.42% to 68.34%. The significant decrease of M-OH suggests that the M-OH groups on the adsorbent surface play an important role in the Sb(V) adsorption process. An increase in the area ratio for the peak at 529.85 eV suggests that M-O groups are forming on the CMO adsorbent surface.

The Mn 2p spectra of the original CMO and after Sb(V) sorption are displayed in Figure 11(b). The Mn $2p_{3/2}$ peak and the Mn $2p_{1/2}$ peak are respectively positioned at 641.7 eV and 653.5 eV, which is in accordance with the spectra of Mn oxides (Ardizzone *et al.* 1998). The spectrum for Mn 2p can be divided into three pairs of doublets, i.e., 640.8 eV, 641.79 eV, and 642.99 eV. The peak at 640.8 eV can be ascribed to the Mn $2p_{3/2}$ of MnO, the peak at 641.79 eV can be assigned to the Mn $2p_{3/2}$ of MnOOH, and the peak at 642.99 eV can be attributed to the Mn $2p_{3/2}$ of MnO_2. The area ratio of the peak at 640.8 eV versus the peak at 642.99 eV is about 1.6:1, i.e., a molar ratio of 2:1 for MnO versus MnO_2, which accords well with the theoretical value of Mn_3O_4 (i.e., 2MnO MnO_2) (An *et al.* 2008). According to the XRD spectra, it can be further demonstrated that the CMO adsorbent consists of MnOOH and Mn_3O_4, which is very well in agreement with the FTIR results. After Sb(V) sorption, the Mn $2p_{3/2}$ spectra showed a minor shift to the lower binding energy. Previous studies of As(V) sorption found that the peak corresponding to Ti $2p_{1/2}$ showed a shift to lower binding energy after As(V) sorption, recommending the formation of Ti-O-As (Li *et al.* 2010). Therefore, it can be deduced that the formation of Mn-O-Sb on the adsorbent surface leads to the Mn-O groups at low binding energies.

The FTIR and XPS analysis as described above suggested that the hydroxyl groups, including on the CMO adsorbent surface and in the MnOOH molecules, played an important role in Sb(V) sorption. The protonation of the hydroxyl groups on the adsorbent and in the MnOOH molecules led to the CMO adsorbent being filled with positive sites in acidic conditions. This promoted absorption of the negative $Sb(OH)_6^-$ on the CMO adsorbent. It was consistent with the pH-dependent sorption results in Figure 6, showing a high adsorption capacity of Sb(V) in acidic or neutral conditions and a clear reduction of adsorption capacity in alkaline conditions. In Figure 7, the Sb(V) removal efficiency varied slightly with the anion concentration, implying the formation of inner-sphere complexes on the adsorbent. The FTIR analysis in Figure 10 demonstrated that the Sb(V) sorption process was heavily related to the Mn-OH groups on the adsorbent surface. The XPS analysis in Figure 11 displayed a reduction of M-OH and an increase of M-O on the adsorbent surface. It deduced that a ligand exchange existing between hydroxyl groups in $Sb(OH)_6^-$ molecules and hydroxyl groups on the adsorbent surface led to the formation of Sb-O-Mn bonds and the release of water molecules. Previous studies have indicated that Sb(V) was adsorbed on metal oxides and oxyhydroxides by the formation of monodentate and bidentate complexes (Sun *et al.* 2018). Previous quantification calculation from the XPS analysis suggested that the stoichiometric ratios of surface hydroxyl between the original adsorbents and target saturated adsorbents were 1:2 for a monodentate surface complex and 2:1 for a bidentate one (Zhang *et al.* 2005). In Figure 10, the ratio value between the surface hydroxyl of CMO and Sb(V)-loaded CMO was 1.53 after Sb(V) adsorption, meaning that both monodentate and bidentate complexes may be involved on the surface of CMO adsorbent in the adsorption of Sb(V).

CONCLUSIONS

A new CMO adsorbent was synthesized by using a simple hydrothermal synthesis method. The synthetic CMO sorbent was mainly an aggregate of Mn_3O_4 nanoparticles and MnOOH nanorods, resulting in the presence of a porous structure to favour the adsorption of target species on its surface. The CMO adsorbent could effectively remove Sb(V). The maximal adsorption capacity of Sb(V) reached 119.63 mg/g at pH 7.0 ± 0.1. Sb(V) adsorption was heavily pH-dependent, since it showed a reduction with increasing pH. The adsorption behaviour of Sb(V) could be well described by the Langmuir isotherm and the pseudo-second-order models. The CMO adsorbent had a good anti-interference ability for coexisting ions and excellent reusability. The hydroxyl groups on the adsorbent and in the MnOOH molecules were responsible for the Sb(V) sorption. Both inner-sphere monodentate and bidentate complexes were formed on the surface of CMO adsorbent in the adsorption of Sb(V).

ETHICS APPROVAL AND CONSENT TO PARTICIPATE

Not applicable.

AVAILABILITY OF DATA AND MATERIALS

The datasets used and/or analysed during the current study are available from the corresponding author on reasonable request.

CONSENT FOR PUBLICATION

The manuscript is approved by all authors for publication.

COMPETING INTERESTS

The authors declare that they have no competing interests.

FUNDING

This work was supported by the National Natural Science Foundation of China (No. 21806034 and No. 52070078), the Natural Science Foundation of Hunan Province (No. 2020JJ5126), and the Scientific Research Program of Hunan Education Department (No. 19C0603 and No. 20C0644).

DATA AVAILABILITY STATEMENT

All relevant data are included in the paper or its Supplementary Information.

REFERENCES

An, G. M., Yu, P., Xiao, M. J., Liu, Z. M., Miao, Z. J., Ding, K. L. & Mao, L. Q. 2008 Low-temperature synthesis of Mn_3O_4 nanoparticles loaded on multi-walled carbon nanotubes and their application in electrochemical capacitors. *Nanotechnology* **19** (27), 1983–1989.

Ardizzone, S., Bianchi, C. L. & Tirelli, D. 1998 Mn_3O_4 and γ-MnOOH powders, preparation, phase composition and XPS characterisation. *Colloid. Surface. A* **134**, 305–312.

Callahan, M. A., Slimak, M. W. & Gabel, N. W. 1979 *Water-Related Environmental Fate of 129 Priority Pollutants. Vol I. EPA 440/4-79-029B*. U.S. Environmental Protection Agency, Washington, DC.

Chen, Y. W., Deng, T. L., Filella, M. & Belzile, N. 2003 Distribution and early diagenesis of antimony species in sediments and porewaters of freshwater lakes. *Environ. Sci. Technol.* **37** (6), 1163–1168.

EEC 1976 *Directive on Pollution Caused by Certain Dangerous Substances Discharged Into the Aquatic Environment of the Community. 76/464/EEC, Pollution Reduction Programmes for List II Substances*, EEC, Brussels.

Elgarahy, A. M., Elwakeel, K. Z., Mohammad, S. H. & Elshoubaky, G. A. 2020 Multifunctional eco-friendly sorbent based on marine brown algae and bivalve shells for subsequent uptake of Congo red dye and copper(II) ions. *J. Environ. Chem. Eng.* **8** (4), 103915–103928.

Elwakeel, K. Z., Elgarahy, A. M., Al-Bogami, A. S., Hamza, M. F. & Guibal, E. 2021 2-Mercaptobenzimidazole-functionalized chitosan for enhanced removal of methylene blue: batch and column studies. *J. Environ. Chem. Eng.* **9** (4), 105609–105621.

Filella, M. & May, P. M. 2003 Computer simulation of the low-molecular-weight inorganic species distribution of antimony(III) and antimony(V) in natural waters. *Geochim. Cosmochim. Acta* **67** (21), 4013–4031.

Filella, M., Belzile, N. & Chen, Y. W. 2002 Antimony in the environment: a review focused on natural waters: i. occurrence. *Earth-Sci. Rev.* **57** (1–2), 125–176.

Foster, R. I., Oh, M., Yang, D., Shon, W. J. & Lee, K. Y. 2019 Antimony(III/V) removal from industrial wastewaters: treatment of spent catalysts formally used in the SOHIO acrylonitrile process. *Water Sci. Technol.* **80** (3), 529–540.

Garba, M., Usman, M., Mazumder, M., Al-Ahmed, A. & Inamuddin 2019 Complexing agents for metal removal using ultrafiltration membranes: a review. *Environ. Chem. Lett.* **17**, 1195–1208.

Guo, X., Wu, Z. & He, M. 2009 Removal of antimony(V) and antimony(III) from drinking water by coagulation-flocculation-sedimentation (CFS). *Water Res.* **43** (17), 4327–4335.

Gupta, A., Chauhan, V. S. & Sankararamakrishnan, N. 2009 Preparation and evaluation of iron-chitosan composites for removal of As(III) and As(V) from arsenic contaminated real life groundwater. *Water Res.* **43** (15), 3862–3870.

He, X. Y., Min, X. B., Peng, T. Y., Ke, Y., Zhao, F. P., Sillanpää, M. & Wang, Y. Y. 2020 Enhanced adsorption of antimonate by ball-milled microscale zero valent iron/pyrite composite: adsorption properties and mechanism insight. *Environ. Sci. Pollut. R.* **27** (14), 16484–16495.

Helfferich, F. 1962 *Ion Exchange*. McGraw-Hill, New York.

Hu, C. C., Wu, Y. T. & Chang, K. H. 2008 Low-temperature hydrothermal synthesis of Mn_3O_4 and MnOOH single crystals: determinant influence of oxidants. *Chem. Mater.* **20** (9), 2890–2894.

Ishii, M., Nakahira, M. & Yamanaka, T. 1972 Infrared absorption spectra and cation distributions in $(Mn, Fe)_3O_4$. *Solid State Commun.* **11** (1), 209–212.

Jia, X. C., Zhou, J. W., Liu, J., Liu, P., Yu, L., Wen, B. & Feng, Y. 2020 The antimony sorption and transport mechanisms in removal experiment by Mn-coated biochar. *Sci. Total Environ.* **724**, 138158–138166.

Jiang, H. L., Tian, L., Chen, P. H., Bai, Y. C., Li, X. Q. & Shu, H. Y. 2020 Efficient antimony removal by self-assembled core-shell nanocomposite of Co_3O_4@rGO and the analysis of its adsorption mechanism. *Environ. Res.* **187**, 109657–109668.

Li, Z., Deng, S., Gang, Y., Huang, J. & Lim, V. C. 2010 As(V) and As(III) removal from water by a Ce–Ti oxide adsorbent: behavior and mechanism. *Chem. Eng. J.* **161** (1–2), 106–113.

Lima, E. C., Hosseini-Bandegharaei, A., Moreno-Piraján, J. C. & Anastopoulos, I. 2018 A critical review of the estimation of the thermodynamic parameters on adsorption equilibria. Wrong use of equilibrium constant in the Van't Hoof equation for calculation of thermodynamic parameters of adsorption. *J. Mol. Liq.* **273**, 425–434.

Liu, R. P., Xu, W., He, Z., Lan, H. C., Liu, H. J., Qu, J. H. & Prasai, T. 2015 Adsorption of antimony(V) onto Mn(II)-enriched surfaces of manganese-oxide and FeMn binary oxide. *Chemosphere* **138** (Nov.), 616–624.

Liu, Y., Lou, Z., Yang, K., Wang, Z. & Xu, X. 2019 Coagulation removal of Sb(V) from textile wastewater matrix with enhanced strategy: comparison study and mechanism analysis. *Chemosphere* **237**, 124494–124503.

Long, X., Wang, X., Guo, X. & He, M. 2020 A review of removal technology for antimony in aqueous solution. *J. Environ. Sci.* **90**, 189–204.

Luo, J. M., Luo, X. B., Crittenden, J., Qu, J. H., Bai, Y. H., Peng, Y. & Li, J. H. 2015a Removal of antimonite (Sb(III)) and antimonate (Sb(V)) from aqueous solution using carbon nanofibers that are decorated with zirconiumoxide (ZrO_2). *Environ. Sci. Technol.* **49**, 11115–11124.

Luo, X., Guo, B., Luo, J., Deng, F., Zhang, S., Luo, S. & Crittenden, J. 2015b Recovery of lithium from wastewater using development of Li ion-imprinted polymers. *ACS Sustain. Chem. Eng.* **3** (3), 460–467.

Mcbride, M. B. 1997 A critique of diffuse double layer models applied to colloid and surface chemistry. *Clays Clay Miner.* **45** (4), 598–608.

Mishra, S., Dwivedi, J., Kumar, A. & Nalini, S. 2016 Removal of antimonite (Sb(III)) and antimonate (Sb(V)) using zerovalent iron decorated functionalized carbon nanotubes. *RSC Adv.* **6**, 95865–95878.

Mitsunobu, S., Takahashi, Y. & Te Rada, Y. 2010 -XANES Evidence for the reduction of Sb(V) to Sb(III) in soil from Sb mine tailing. *Environ. Sci. Technol.* **44** (4), 1281–1287.

Mosivand, S., Monzon, L., Kazeminezhad, I., Kumar, A. & Coey, J. 2018 Pulsed electrochemical and electroless techniques for efficient removal of Sb and Pb from water. *Environ. Sci-Wat. Res. Technol.* **4** (12), 2179–2190.

Nepel, T., Landers, R., Vieira, M. & Neto, A. 2019 Metallic copper removal optimization from real wastewater using pulsed electrodeposition. *J. Hazard. Mater.* **384**, 121416–121425.

Park, T., Ampunan, V., Maeng, S. & Chung, E. 2017 Application of steel slag coated with sodium hydroxide to enhance precipitation-coagulation for phosphorus removal. *Chemosphere* **167**, 91–97.

Qi, Z. L., Joshi, T. P., Liu, R. P., Liu, H. J. & Qu, J. H. 2017 Synthesis of Ce(III)-doped Fe_3O_4 magnetic particles for efficient removal of antimony from aqueous solution. *J. Hazard. Mater.* **329**, 193–204.

Qiu, C., Frantisek, M., Alexander, D. T., Moritz, S. & Thomas, T. 2018 In situ structural study of Sb(V) adsorption on hematite (1102) using X-ray surface scattering. *Environ. Sci. Technol.* **52** (19), 11161–11168.

Scheinost, A. C., Rossberg, A., Vantelon, D., Xifra, I., Kretzschmar, R., Leuz, A. K., Funke, H. & Johnson, C. A. 2006 Quantitative antimony speciation in shooting-range soils by EXAFS spectroscopy. *Geochim. Cosmochim. Acta.* **70** (13), 3299–3312.

Shalaby, S. M., Madkour, F. F., El-Kassas, H. Y., Mohamed, A. A. & Elgarahy, A. M. 2021 Green synthesis of recyclable iron oxide nanoparticles using *Spirulina platensis* microalgae for adsorptive removal of cationic and anionic dyes. *Environ. Sci. Pollut. R.* **28**, 65549–65572.

Sun, Q., Liu, C., Alves, M. E., Ata-Ul-Karim, S. T. & Wang, Y. J. 2018 The oxidation and sorption mechanism of Sb on δ-MnO_2. *Chem. Eng. J.* **342**, 429–437.

Sundar, S. & Chakravarty, J. 2010 Antimony toxicity. *Int. J. Env. Res. Pub. He.* **7** (12), 4267–4277.

Thanabalasingam, P. & Pickering, W. F. 1990 Specific sorption of antimony (III) by the hydrous oxides of Mn. Fe, and Al. *Water Air Soil Poll.* **49** (1), 175–185.

USEPA 2009 *List of Drinking Water Contaminants and Their Maximum Contaminant Levels*. US EPA, Washington, DC, USA.

Wang, X., He, M., Xi, J. & Lu, X. 2011 Antimony distribution and mobility in rivers around the world's largest antimony mine of Xikuangshan, Hunan Province, China. *Microchem. J.* **97** (1), 4–11.

Wang, J., Chen, J., Li, Q. & Zhang, G. 2019a Novel nanostructured Fe–Cu–Al trimetal oxide for enhanced antimony(V) removal: synthesis, characterization and performance. *Water Sci. Technol.* **79** (10), 1995–2004.

Wang, L., Wang, J. Y., Wang, Z. X., Feng, J. T., Li, S. S. & Yan, W. 2019b Synthesis of Ce-doped magnetic biochar for effective Sb(V) removal: performance and mechanism. *Powder Technol.* **345**, 501–508.

Weber, W. J. & Morris, J. C. 1963 Kinetics of adsorption on carbon from solution. *J. Sanit. Eng. Div.* **89**, 31–59.

Wedepohl, K. H. 1995 The composition of the continental crust. *Geochim. Cosmochim. Acta* **59** (7), 1217–1232.

Xu, W., Wang, H. J., Liu, R. P., Zhao, X. & Qu, J. H. 2011 The mechanism of antimony (III) removal and its reactions on the surfaces of Fe-Mn binary oxide. *J. Colloid Interface Sci.* **363** (1), 320–326.

Yang, L., She, Q., Wan, M. P., Wang, R., Chang, W. C. & Tang, C. Y. 2017 Removal of haloacetic acids from swimming pool water by reverse osmosis and nanofiltration. *Water Res.* **116**, 116–125.

Ye, T., Min, W., Liu, R., Li, Y., Wang, D., Tan, J., Wu, R. & Huang, Y. 2011 Electrospun membrane of cellulose acetate for heavy metal ion adsorption in water treatment. *Carbohydr. Polym.* **83** (2), 743–748.

Zhang, W., Yang, Z., Yi, L., Tang, S., Han, X. & Min, C. 2004 Controlled synthesis of Mn_3O_4 nanocrystallites and MnOOH nanorods by a solvothermal method. *J. Cryst. Growth* **263** (1–4), 394–399.

Zhang, Y., Yang, M., Dou, X., He, H. & Wang, D. 2005 Arsenate adsorption on an Fe-Ce bimetal oxide adsorbent: role of surface properties. *Environ. Sci. Technol.* **39** (18), 7246–7253.

Zhang, W., Zhang, G. S., Liu, C. H., Li, J., Zheng, T., Ma, J., Wang, L., Jiang, J. & Zhai, X. D. 2018 Enhanced removal of arsenite and arsenate by a multifunctional Fe-Ti-Mn composite oxide: photooxidation, oxidation and adsorption. *Water Res.* **147** (15), 264–275.

Zhao, T. H., Tang, Z., Zhao, X. L., Zhang, H., Wang, J. Y., Wu, F. C., Giesy, J. P. & Shi, J. 2019 Efficient removal of both antimonite (Sb(III)) and antimonate (Sb(V)) from environmental water using titanate nanotubes and nanoparticles. *Environ. Sci-Nano* **6**, 834–850.

Zou, J. P., Liu, H. L., Luo, J., Xing, Q. J. & Suib, S. L. 2016 Three-dimensional reduced graphene oxide coupled with Mn_3O_4 for highly efficient removal of Sb(III) and Sb(V) from water. *ACS Appl. Mater. Inter.* **8** (28), 18140–18149.

First received 5 January 2022; accepted in revised form 29 March 2022. Available online 15 April 2022